INTERNATIONAL JOURNAL FOR NUMERICAL METHODS IN FLUIDS, VOL. 22, 619–641 (1996)

ON THE CONSTRUCTION OF A THIRD-ORDER ACCURATE MONOTONE CONVECTION SCHEME WITH APPLICATION TO TURBULENT FLOWS IN GENERAL DOMAINS

M. ZIJLEMA

Faculty of Technical Mathematics and Informatics, Delft University of Technology, PO Box 5031, 2600 GA Delft, The Netherlands

SUMMARY

A formally third-order accurate finite volume upwind scheme which preserves monotonicity is constructed. It is based on a third-order polynomial interpolant in Leonard's normalized variable space. A flux limiter is derived using the fact that there exists a one-to-one map between normalized variable and TVD spaces. This scheme, which is relatively simple and quite compact, is implemented in a staggered general co-ordinates finite volume algorithm including the standard k–ε model and applied to the turbulence transport equations. A number of test problems demonstrate the utility of the proposed scheme. It is shown that in cases where turbulence convection is dominant, the application of a higher-order monotone convection scheme to the turbulence equations leads to results which are more accurate than those obtained using the first-order upwind scheme.

KEY WORDS: convective transport; monotonicity; finite volume; boundary-fitted co-ordinates; turbulence modelling

1. INTRODUCTION

Approximation of convective transport is still one of the unresolved issues of CFD. The main problem is to combine accuracy, stability, monotonicity preservation, economy and algebraic simplicity. In principle, convection may be discretized by central differences because of second-order accuracy. However, if the mesh Peclet number is sufficiently large, non-physical numerical oscillations called 'wiggles' may occur and thus accuracy and stability of the solution process may be impaired. In order to avoid the instability and non-monotonicity associated with central differencing, first-order upwind differencing is often used. The stability inherent in this scheme has made it popular. Unfortunately, this method introduces an error, which has the form of a viscous term with artificial viscosity. In high-Reynolds-number flows this artificial viscosity dominates the physical viscosity and the solution produced is much smoother than the correct one. Furthermore, because the interpolation used in evaluating unknown fluxes is between sets of nodes along grid lines, significant numerical errors arise when the flow direction is not aligned with those lines. Hence it is necessary to minimize numerical diffusion (both truncation error and cross-flow diffusion), especially in situations when turbulence model deficiencies have to be identified. Grid refinement is the traditional way to reduce the numerical diffusion errors. However, improvement in accuracy by grid refinement is not always possible, particularly in three-dimensional applications, owing to excessive storage and run time requirements.

Because of the disadvantages of the first-order upwind approximation mentioned above, a number of schemes which retain the stability of first-order upwind differencing while providing higher-order

CCC 0271–2091/96/070619–23

Received 5 December 1994
Revised 31 March 1995

accuracy or leading to less numerical diffusion have been proposed. The most well-known and often employed schemes with these properties are the second-order linear upwind scheme (LUDS), the third-order upstream-weighted quadratic interpolation scheme (QUICK) proposed by Leonard[1] and the skew upwind differencing scheme (SUDS) suggested by Raithby.[2]

Like central schemes, all higher-order linear upwind schemes are non-monotone. This means that they may give rise to unphysical oscillations, typically in the vicinity of steep gradients of a quantity to be resolved. For linear and weakly coupled equations this feature is no more than a small optical defect. However, in strongly coupled and non-linear situations at high Reynolds numbers these numerical oscillations tend to grow in an unbounded manner, which prevents the solutions from converging. This tendency must be regarded as a serious limitation with respect to the turbulence model equations, which are generally highly non-linear, and the coupling between these equations is often strong. It is for this reason that the convective transport of turbulence, occurring e.g. in k–ε-type models, has been approximated with highly stable first-order upwind schemes in numerous publications. Otherwise, physically and numerically undesirable features such as negative turbulent kinetic energy may arise in high-gradient regions. Hence, although the use of higher-order schemes is essential whenever turbulence convection has to be accurately resolved, monotonicity must be ensured.

Over the past two decades there have been many attempts to devise higher-order convection schemes which do not exhibit spurious oscillations. Some well-known types of such schemes have been developed and evaluated for practical flow computations. In 1983 Harten[3] laid a rigorous mathematical foundation for the construction of non-linear higher-order upwind schemes which preserves monotonicity, based on the total variation diminishing (TVD) concept. Such schemes cannot create new local extrema, whereas the value of an existing local minimum cannot be decreased and that of a local maximum cannot be increased. Different TVD schemes arise by introducing different limiters. Sweby[4] has derived some constraints for a second-order accurate scheme to be TVD and has also introduced a TVD diagram which encloses a wide range of flux limiters such as those of Van Leer, Roe ('superbee' limiter) and Chakravarthy and Osher. An overview of TVD schemes with several flux limiters can be found in Reference 5 and recently in Reference 6. TVD schemes are used widely in compressible Euler and Navier–Stokes codes for capturing shocks and flow discontinuities and have been shown to give satisfactory results in many cases.

Another method which also removes unphysical numerical oscillations from the solutions of higher-order schemes is based on switching from one scheme to another controlled by a convection boundedness criterion, proposed by Gaskell and Lau.[7] The construction is based on devising non-linear characteristics in the so-called normalized variable (NV) diagram.[8] Examples are the SHARP scheme formulated by Leonard[8] and the SMART scheme of Gaskell and Lau.[7] Both are monotone versions of the QUICK scheme. The construction of the former scheme is based on exponential NV characteristics, whereas the latter is constructed with piecewise linear NV characteristics. Both schemes have been shown to give higher-order accurate oscillation-free solutions of simple linear transport problems. However, a disadvantage of these schemes is the fact that they contain many conditional statements and are therefore non-vectorizable. Furthermore, they have a high computational cost in comparison with other higher-order schemes. For example, according to Tamamidis and Assanis,[9] the SHARP scheme requires about seven times more CPU time than QUICK for a simple test problem on a 100×100 grid.

The method of constructing a monotone scheme presented in this paper is based on the fact that the NV characteristics can be recast in terms of flux limiters.[8] First a polynomial NV characteristic of order three in the normalized variable diagram is constructed in order to obtain a third-order accurate monotone scheme in the finite volume formulation. Using the unique relationship between NV and TVD spaces, this scheme is rewritten as a flux-limited scheme called ISNAS (Interpolation Scheme which is Non-oscillatory for Advected Scalars). The reason for employing the TVD rather than NV formalism is that it can be easily implemented by means of the deferred correction approach using flux limiters without enlarging a stencil.

In what follows, a short outline of the mathematical formulation of the ISNAS scheme is given. This scheme is implemented in the ISNAS (Information System for the Navier–Stokes equations) code[10] applicable to laminar and turbulent flows in arbitrarily shaped domains, which is based on a co-ordinate-invariant finite volume discretization on a staggered non-orthogonal grid of the incompressible Navier–Stokes equations. Turbulence is modelled by the standard k–ε eddy viscosity closure. Results are presented which demonstrate the scheme's performance in linear and non-linear cases.

2. MATHEMATICAL FORMULATION

2.1. *Fundamentals of Leonard's normalized variable concept*

We consider advective transport of a scalar field, which can be written as

$$\frac{\partial u_\alpha \phi}{\partial x_\alpha} = 0, \quad \alpha \in \{1, 2, \dots, d\}, \tag{1}$$

where ϕ is the scalar field, u_α is the velocity component of a flow field in the x_α-direction, d is a given space dimension and the summation convention is used. Note that (1) can easily be extended to general co-ordinates, but for the sake of clarity we restrict ourselves to the Cartesian tensorial form. Moreover, without loss of generality, $d = 2$. Discretization of (1) is carried out using the standard finite volume technique on a staggered grid as depicted in Figure 1:

$$\int_\Omega \frac{\partial u_\alpha \phi}{\partial x_\alpha} \mathrm{d}x_1 \mathrm{d}x_2 \approx u_1 \phi \Big|_{(i-1/2,j)}^{(i+1/2,j)} \Delta x_2 + u_2 \phi \Big|_{(i,j-1/2)}^{(i,j+1/2)} \Delta x_1, \tag{2}$$

where Δx_α is the grid size of the control volume in the x_α-direction. To simplify the following consideration, we take $\Delta x_1 = \Delta x_2$.

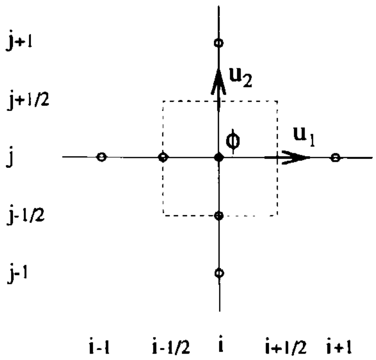

Figure 1. Two-dimensional staggered finite volume

Approximation of the face values of ϕ can be done in several ways. A widespread approach is the first-order upwind method (for the evaluation of $\phi_{(i+1/2,j)}$, for example):

$$\phi_{(i+1/2,j)} = \phi_{(i,j)}, \quad \text{if } u_1|_{(i+1/2,j)} > 0, \tag{3}$$

$$\phi_{(i+1/2,j)} = \phi_{(i+1,j)}, \quad \text{if } u_1|_{(i+1/2,j)} < 0. \tag{4}$$

This scheme is first-order accurate and monotone. However, it produces excessive numerical diffusion and can often not be employed. Another method is to approximate the face value $\phi_{(i+1/2,j)}$ with Leonard's QUICK scheme[1]:

$$\phi_{(i+1/2,j)} = \tfrac{1}{2}(\phi_{(i,j)} + \phi_{(i+1,j)}) - \tfrac{1}{8}(\phi_{(i-1,j)} - 2\phi_{(i,j)} + \phi_{(i+1,j)}), \quad \text{if} \quad u_1|_{(i+1/2,j)} > 0, \tag{5}$$

$$\phi_{(i+1/2,j)} = \tfrac{1}{2}(\phi_{(i,j)} + \phi_{(i+1,j)}) - \tfrac{1}{8}(\phi_{(i,j)} - 2\phi_{(i+1,j)} + \phi_{(i+2,j)}), \quad \text{if} \quad u_1|_{(i+1/2,j)} < 0. \tag{6}$$

This scheme is third-order accurate in the case of a uniform grid, but it is non-monotone, so that for flows with sharp gradients it may produce oscillatory solutions.

In order to construct a higher-order scheme which enforces monotonicity, Leonard[8] introduced variable normalization, while Gaskell and Lau[7] proposed a convection boundedness criterion. We shall give a brief description. We consider the control volume surrounding the point (i, j) as shown in Figure 1 and assume that $u_1|_{(i+1/2,j)} > 0$. A normalized variable (NV) $\hat{\phi}$ at the point $(i+k, j)$ is defined as

$$\hat{\phi}_{(i+k,j)} = \frac{\phi_{(i+k,j)} - \phi_{(i-1,j)}}{\phi_{(i+1,j)} - \phi_{(i-1,j)}}, \quad k = -1, -\tfrac{1}{2}, 0, \tfrac{1}{2}, 1. \tag{7}$$

Hence $\hat{\phi}_{(i-1,j)} = 0$ and $\hat{\phi}_{(i+1,j)} = 1$. With this definition, several upwind schemes can be rewritten in a more simplified form. For example, QUICK may be written as

$$\hat{\phi}_{(i+1/2,j)} = \tfrac{1}{2}(\hat{\phi}_{(i,j)} + 1) - \tfrac{1}{8}(-2\hat{\phi}_{(i,j)} + 1) = \tfrac{3}{4}\hat{\phi}_{(i,j)} + \tfrac{3}{8}, \tag{8}$$

whereas the first-order upwind scheme in terms of normalized variables is simply

$$\hat{\phi}_{(i+1/2,j)} = \hat{\phi}_{(i,j)}. \tag{9}$$

Both schemes depend linearly on $\hat{\phi}_{(i,j)}$. This dependence is shown diagrammatically in Figure 2. The curves shown are called NV characteristics.

Using Taylor expansion, one can show that for any scheme based on linear or non-linear NV characteristics, the following two properties hold.

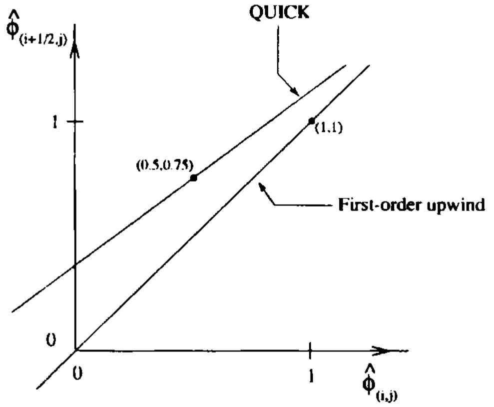

Figure 2. NV diagram with two well-known characteristics

1. A scheme with an NV characteristic that passes through the point $(\frac{1}{2}, \frac{3}{4})$ in the NV diagram is second-order accurate.
2. A scheme with an NV characteristic that has a slope of $\frac{3}{4}$ while passing through the point $(\frac{1}{2}, \frac{3}{4})$ is third-order accurate.

For the construction of a monotone scheme we use the following important criterion formulated by Gaskell and Lau.[7]

Convection boundedness criterion

Given a continuous or piecewise continuous NV characteristic

$$f: \hat{\phi}_{(i,j)} \rightarrow \hat{\phi}_{(i+1/2,j)},$$

the corresponding scheme is monotonicity-preserving if and only if

(i) $\forall \hat{\phi}_{(i,j)} \in [0, 1], \quad \hat{\phi}_{(i,j)} \leqslant f(\hat{\phi}_{(i,j)}) \leqslant 1$

(ii) $\forall \hat{\phi}_{(i,j)} \notin [0, 1], \quad \hat{\phi}_{(i+1/2,j)} = f(\hat{\phi}_{(i,j)}) = \hat{\phi}_{(i,j)}$

(iii) $f(0) = 0$ and $f(1) = 1$.

It is clear that the NV characteristic associated with a higher-order monotone scheme must be non-linear or piecewise linear. For example, the SMART scheme of Gaskell and Lau is based on piecewise linear NV characteristics, whereas Leonard constructed the SHARP scheme which is represented by a blend of piecewise linear and exponential NV characteristics. Note that SHARP does not fully obey the convection boundedness criterion (CBC). The next subsection gives a short outline of the construction of a third-order scheme which satisfies the above criteria.

2.2. *A third-order accurate interpolation scheme which is non-oscillatory for advected scalars*

The idea behind the construction of the third-order accurate ISNAS scheme is to derive a third-order polynomial which passes through the points (0, 0), (1, 1) and $(\frac{1}{2}, \frac{3}{4})$ while having a slope of $\frac{3}{4}$ at $(\frac{1}{2}, \frac{3}{4})$. We find the third-order polynomial

$$\hat{\phi}_{(i+1/2,j)} = \hat{\phi}^3_{(i,j)} - \tfrac{5}{2}\hat{\phi}^2_{(i,j)} + \tfrac{5}{2}\hat{\phi}_{(i,j)}. \tag{10}$$

Hence the resulting NV characteristic which satisfies the above criteria reads

$$\hat{\phi}_{(i+1/2,j)} = \begin{cases} \hat{\phi}_{(i,j)}, & \hat{\phi}_{(i,j)} < 0, \\ \hat{\phi}^3_{(i,j)} - \frac{5}{2}\hat{\phi}^2_{(i,j)} + \frac{5}{2}\hat{\phi}_{(i,j)}, & 0 \leqslant \hat{\phi}_{(i,j)} \leqslant 1, \\ \hat{\phi}_{(i,j)}, & \hat{\phi}_{(i,j)} > 1. \end{cases} \tag{11}$$

This non-linear NV characteristic is shown in Figure 3.

The corresponding flux-limited scheme is derived as follows. First, (10) is rewritten as

$$\hat{\phi}_{(i+1/2,j)} = \hat{\phi}_{(i,j)} + \tfrac{1}{2}(3\hat{\phi}_{(i,j)} - 2\hat{\phi}^2_{(i,j)})(1 - \hat{\phi}_{(i,j)}). \tag{12}$$

In terms of unnormalized variables this equation (12) simply reads

$$\phi_{(i+1/2,j)} = \phi_{(i,j)} + \tfrac{1}{2}\Psi(r_{(i+1/2,j)})(\phi_{(i+1,j)} - \phi_{(i,j)}), \tag{13}$$

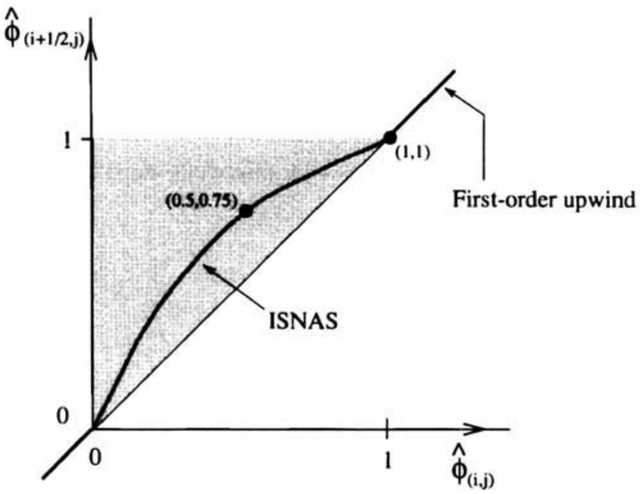

Figure 3. NV characteristic associated with ISNAS scheme in CBC region

where Ψ is a flux limiter to be derived and the limiter argument $r_{(i+1/2,j)}$ is the ratio of two consecutive solution gradients defined by

$$r_{(i+1/2,j)} = \frac{\phi_{(i,j)} - \phi_{(i-1,j)}}{\phi_{(i+1,j)} - \phi_{(i,j)}}. \tag{14}$$

Using (7), this ratio can be expressed in terms of normalized variables as

$$r_{(i+1/2,j)} = \frac{\hat{\phi}_{(i,j)}}{1 - \hat{\phi}_{(i,j)}}. \tag{15}$$

From (12) and (15) we deduce the flux limiter

$$\Psi(r) = \frac{r^2 + 3r}{(1 + r)^2}, \quad r \geqslant 0. \tag{16}$$

With (11), (13) and (15) it follows that for all $r < 0$, $\Psi(r) = 0$. Hence the flux limiter associated with scheme (13), which is equivalent to (11), is given by

$$\Psi(r) = \tfrac{1}{2}(r + |r|)\frac{r + 3}{(1 + r)^2}. \tag{17}$$

The TVD diagram corresponding to the limiter (17) is given in Figure 4, which shows that Sweby's monotonicity preservation conditions[4] are slightly violated, because $\Psi'(r) = 3 > 2$ for $r \downarrow 0$. This can be expected, because the convection boundedness criterion is weaker and thus more flexible than Sweby's TVD criterion. We also note that $\Psi(1) = 1$, which is necessary for a scheme to be at least second-order accurate.[4] Moreover, it can be shown for an arbitrary limiter Ψ that $\Psi'(1) = \frac{1}{4}$ is necessary and sufficient for third-order accuracy of the flux (see Appendix). Indeed, the slope of the ISNAS limiter (17) for $r = 1$ is $\frac{1}{4}$. In conclusion, the proposed limiter has the advantage of being a smooth function of r for $r > 0$, so that it may offer better convergence behaviour.

3. INVARIANT DISCRETIZATION AND NUMERICAL FRAMEWORK

The incompressible Navier–Stokes equations and a transport equation for any scalar quantity ϕ (including turbulent quantities k and ε) are solved numerically using a finite volume technique in

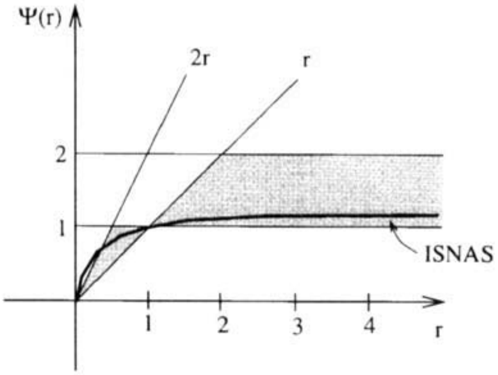

Figure 4. Flux limiter diagram for ISNAS limiter

general boundary-fitted co-ordinates on a staggered grid. The governing equations have to be recast in a form in which both independent and dependent variables are invariant with respect to a change in co-ordinates. In this paper the invariant discretization of a transport equation for scalar ϕ is outlined. Details of the discretization of the momentum equations can be found e.g. in Reference 11.

Using tensor notation in general co-ordinates, the transport equation for scalar ϕ is written as

$$\frac{\partial \rho\phi}{\partial t} + (\rho U^{\alpha}\phi)_{,\alpha} - (\kappa_{\phi} g^{\alpha\beta}\phi_{,\beta})_{,\alpha} = S_{\phi}, \tag{18}$$

where ρ is the density, U^{α} is the contravariant velocity component and S_{ϕ} denotes a source term which may depend on ϕ and U^{α}. Furthermore, κ_{ϕ} is a diffusion coefficient and $g^{\alpha\beta}$ is the contravariant metric tensor defined as

$$g^{\alpha\beta} = \mathbf{a}^{(\alpha)} \cdot \mathbf{a}^{(\beta)}, \tag{19}$$

where

$$\mathbf{a}^{(\alpha)} = \frac{\partial \xi^{\alpha}}{\partial \mathbf{x}} \tag{20}$$

is the contravariant base vector with respect to the mapping

$$T\colon \mathbf{x} = \mathbf{x}(\boldsymbol{\xi}). \tag{21}$$

Here $\mathbf{x}$ represents the Cartesian co-ordinates and $\boldsymbol{\xi}$ the boundary-conforming curvilinear co-ordinates. The mapping is assumed to be regular, i.e. the Jacobian of the transformation, denoted $\sqrt{g}$, does not vanish. For convenience, equation (18) is written in the form

$$Q^{\alpha}_{,\alpha} = S_{\phi} - \frac{\partial \rho\phi}{\partial t}, \tag{22}$$

where

$$Q^{\alpha} = \rho U^{\alpha}\phi - \kappa_{\phi} g^{\alpha\beta}\phi_{,\beta}. \tag{23}$$

Furthermore, we introduce the local cell co-ordinates given by Figure 5. We have a uniform grid with unit mesh widths in $\boldsymbol{\xi}$-space. Discretization of (22) is obtained by integration over a finite volume Ω with centre (i, j) using the identity

$$Q^{\alpha}_{,\alpha} = \frac{1}{\sqrt{g}} \frac{\partial \sqrt{g} Q^{\alpha}}{\partial \xi^{\alpha}}. \tag{24}$$

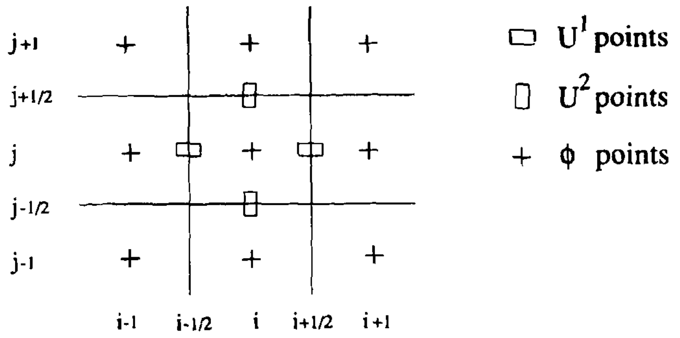

Figure 5. Local cell co-ordinates

This yields

$$\int_\Omega Q^\alpha_{,\alpha} \mathrm{d}\Omega \approx \sqrt{g}Q^1|^{(i+1/2,j)}_{(i-1/2,j)} + \sqrt{g}Q^2|^{(i,j+1/2)}_{(i,j-1/2)}. \tag{25}$$

The right-hand side of (22) is integrated using the midpoint rule:

$$\int_\Omega \left(S_\phi - \frac{\partial \rho\phi}{\partial t}\right)\mathrm{d}\Omega \approx \sqrt{g_{(i,j)}}\left(S_\phi - \frac{\partial \rho\phi}{\partial t}\right)|_{(i,j)}. \tag{26}$$

The discretization is completed by substituting (23) into (25) and approximating the cell face values (advection) and derivatives (diffusion) appropriately. Approximation of cell face derivatives has been carried out with second-order central differences. The advective cell face values are approximated by the first-order upwind scheme, which is corrected by adding an appropriate antidiffusive flux controlled by a limiter. For example, approximation of $\phi_{(i+1/2,j)}$ gives

$$\phi_{(i+1/2,j)} = \phi_{(i,j)} + \tfrac{1}{2}\Psi(r^+_{(i+1/2,j)})(\phi_{(i+1,j)} - \phi_{(i,j)}) \quad \text{if} \quad U^1_{(i+1/2,j)} \geqslant 0, \tag{27}$$

$$\phi_{(i+1/2,j)} = \phi_{(i+1,j)} - \tfrac{1}{2}\Psi(r^-_{(i+1/2,j)})(\phi_{(i+1,j)} - \phi_{(i,j)}) \quad \text{if} \quad U^1_{(i+1/2,j)} < 0, \tag{28}$$

where

$$r^+_{(i+1/2,j)} = \frac{\phi_{(i,j)} - \phi_{(i-1,j)}}{\phi_{(i+1,j)} - \phi_{(i,j)}}, \qquad r^-_{(i+1/2,j)} = \frac{\phi_{(i+1,j)} - \phi_{(i+2,j)}}{\phi_{(i,j)} - \phi_{(i+1,j)}}. \tag{29}$$

Because $\Psi(r)$ is by definition non-linear, this scheme is implemented in a deferred correction manner:

$$\phi^{n+1}_{(i+1/2,j)} = \phi^{\mathrm{F},n+1}_{(i+1/2,j)} + (\phi^{\mathrm{H},n}_{(i+1/2,j)} - \phi^{\mathrm{F},n}_{(i+1/2,j)}), \tag{30}$$

where n represents the time level and 'F' and 'H' indicate the first-order upwind and higher-order schemes respectively. The first-order upwind scheme for the evaluation of ϕ at the point $(i + 1/2, j)$, for example, is given by

$$\phi_{(i+1/2,j)} = \tfrac{1}{2}[1 + \mathrm{sign}(U^1_{(i+1/2,j)})]\phi_{(i,j)} + \tfrac{1}{2}[1 - \mathrm{sign}(U^1_{(i+1/2,j)})]\phi_{(i+1,j)}. \tag{31}$$

The discretization of the transport equation results in the nine-point stencil presented in Figure 5.

Marching in time is done with the implicit Euler technique, whereas the pressure is obtained from a pressure correction equation derived from a combination of the continuity and momentum equations, as described by van Kan.[12] The discretized set of equations is solved iteratively using the GMRES method. The standard k–ε model in conjunction with wall functions[13] is employed for modelling turbulence. For further details see References 11 and 14.

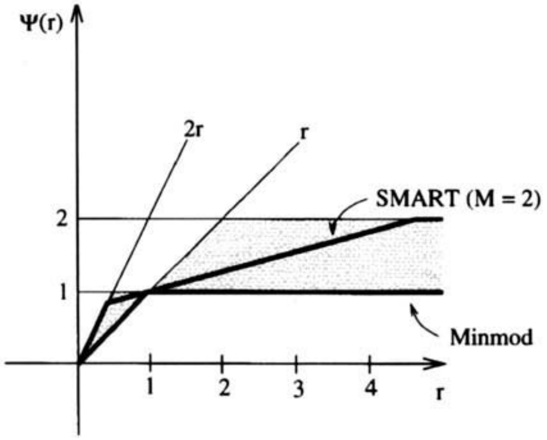

Figure 6. Flux limiter diagram for Minmod and SMART

4. TEST PROBLEMS AND RESULTS

To investigate the properties of the ISNAS scheme described in Section 2.2, two linear and two non-linear test cases have been examined. The first two cases involve advection dominance and steep gradients of the transported scalars, whereas in the last two cases the k–ε model is employed, which is our primary interest. For comparison, the first-order upwind (UDS, $\Psi=0$), QUICK ($\Psi(r)=\frac{3}{4}+\frac{1}{4}r$), Roe's 'Minmod' limiter[4] and SMART[7] are included. The Minmod limiter, which is known to be the most diffusive one, is given by

$$\Psi(r)=\mathrm{minmod}(r,1)=\max(0,\min(r,1)),\tag{32}$$

whereas SMART is given by

$$\Psi(r)=\max(0,\min(M,\tfrac{3}{4}+\tfrac{1}{4}r,2r)),\quad M=4.\tag{33}$$

With a large value of M we obtain more accuracy near sharp gradients. However, in this paper the value is changed to $M=2$, which gives much better convergence behaviour than the original SMART scheme. See Figure 6.

4.1. Unsteady rotation of a cone-shaped scalar field

A two-dimensional solid body rotation test* is performed to investigate the accuracy, monotonicity and conservation behaviour of the five schemes discussed. A scalar cone field is advected around by a stationary velocity field:

$$\frac{\partial\phi}{\partial t}+u\frac{\partial\phi}{\partial x}+v\frac{\partial\phi}{\partial y}=0,\quad (x,y)\in[-1,1]\times[-1,1],\tag{34}$$

with

$$(u,v)=(-2\pi y,2\pi x).\tag{35}$$

The initial cone field is given by

$$\phi(x,y,0)=0\cdot01^{4[(x+\frac{1}{2})^2+y^2]}.\tag{36}$$

---

* Also known as the Molenkamp test.

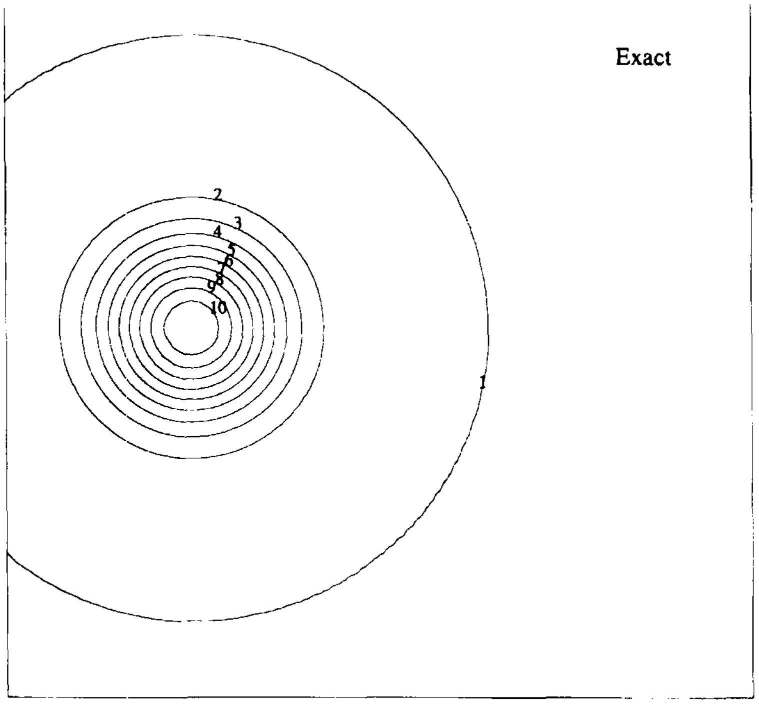

Figure 7. Contour plot of exact solution after one full rotation with levels $10^{-5} + 0{\cdot}1(n-1), n = 1, 2, \ldots, 10$

On the boundaries the following inflow conditions are imposed:

$$\begin{aligned} \phi(-1, y, t) &= 0{\cdot}01^{4\{[-1+\frac{1}{2}\cos(2\pi t)]^2+[y+\frac{1}{2}\sin(2\pi t)]^2\}}, \quad y \in [-1, 0], \\ \phi(1, y, t) &= 0{\cdot}01^{4\{[1+\frac{1}{2}\cos(2\pi t)]^2+[y+\frac{1}{2}\sin(2\pi t)]^2\}}, \quad y \in [0, 1], \\ \phi(x, -1, t) &= 0{\cdot}01^{4\{[x+\frac{1}{2}\cos(2\pi t)]^2+[-1+\frac{1}{2}\sin(2\pi t)]^2\}}, \quad x \in [0, 1], \\ \phi(x, 1, t) &= 0{\cdot}01^{4\{[x+\frac{1}{2}\cos(2\pi t)]^2+[1+\frac{1}{2}\sin(2\pi t)]^2\}}, \quad x \in [-1, 0]. \end{aligned} \tag{37}$$

More details can be found in Reference 15.

Computations have been performed on an 80 × 80 grid and for accuracy reasons the Crank–Nicolson scheme has been chosen, in which the time step is taken sufficiently small to ensure monotonicity. Note that Crank–Nicolson is not applied to the deferred correction (30). The exact solution after one full rotation, which is identical with the Gaussian initial field (36), is presented in Figure 7 and the numerical results in Figure 8. It is clear that the solution obtained with the UDS scheme is extremely inaccurate. On the other hand, the monotone schemes and QUICK dramatically improve the results. Since the isoline $\phi(x, y, t) = 10^{-5}$ is also plotted, it is clear that none of the schemes produces this isoline accurately.

Some quantities are measured in order to quantify the error of the five schemes. The L_2-norm of the difference between the exact and numerical solutions is defined by

$$\| \Delta\phi \|_2 = \frac{\sqrt{\left(\sum_{i=1}^{N} (\phi_{i,\text{exact}} - \phi_{i,\text{numerical}})^2\right)}}{N}, \tag{38}$$

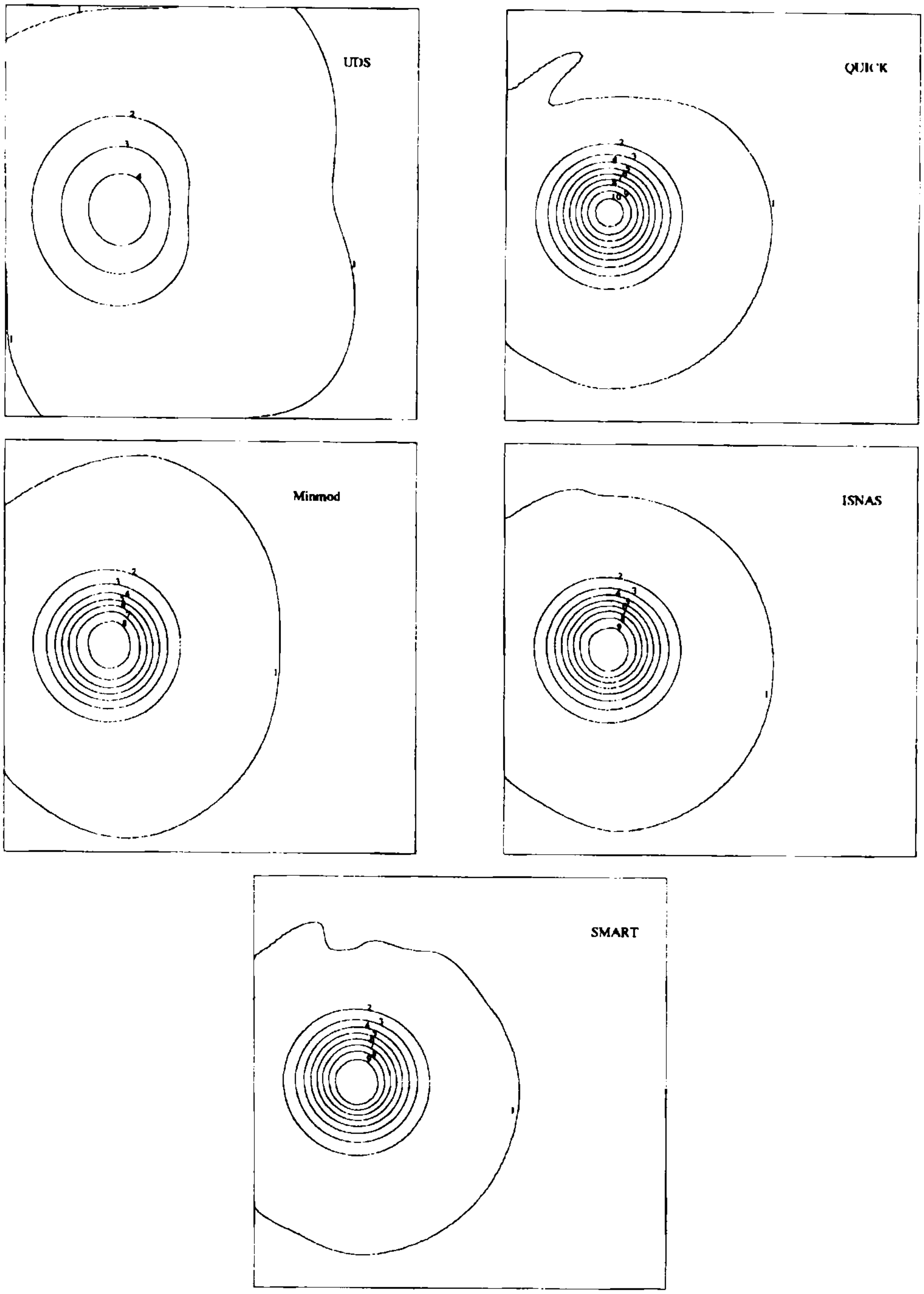

Figure 8. Contour plots of scalar property with levels $10^{-5} + 0\cdot 1(n-1), n = 1, 2, \ldots, 10$, obtained with various schemes on 80×80 grid

where N is the number of grid points, whereas the L_∞-norm of the solution error is defined as

$$\| \Delta\phi \|_\infty = \max_{1 \leqslant i \leqslant N} |\phi_{i,\text{exact}} - \phi_{i,\text{numerical}}|. \tag{39}$$

Furthermore, monotonicity and conservation of the schemes are examined respectively by

$$\phi_{\min} = \min_{1 \leqslant i \leqslant N} \phi_{i,\text{numerical}} \tag{40}$$

and

$$|1 - r_{\text{mass}}| = \left| 1 - \frac{\sum_{i=1}^{N} \phi_{i,\text{numerical}}}{\sum_{i=1}^{N} \phi_{i,\text{exact}}} \right|. \tag{41}$$

More details on these quantities and the motivation for their use can be found in Reference 15, in which also an evaluation of a wide variety of upwind schemes for this specific problem is documented. The quantities are measured on three different grids: 20 × 20, 40 × 40 and 80 × 80. The measurements of these quantities for all schemes are summarized in Table I.

Defining h as the maximal grid width and considering the ISNAS scheme, the solution errors behave in between $\mathcal{O}(h^2)$ and $\mathcal{O}(h^3)$ with respect to $\| \Delta\phi \|_2$, while $\| \Delta\phi \|_\infty$ behaves $\mathcal{O}(h)$. Furthermore, the convergence of $\| \Delta\phi \|_2$ tends to $\mathcal{O}(h^3)$ for $h \downarrow 0$. The same hold for SMART, which converges a little faster than ISNAS. Regarding the QUICK scheme, $\| \Delta\phi \|_\infty$ behaves in between $\mathcal{O}(h)$ and $\mathcal{O}(h^2)$, whereas $\| \Delta\phi \|_2$ tends to $\mathcal{O}(h^3)$ for $h \downarrow 0$. In the case of Minmod the $\| \Delta\phi \|_2$ convergence tends to $\mathcal{O}(h^2)$. Clearly, as expected, UDS yields an $\mathcal{O}(h)$ convergence. Of the monotone schemes, SMART yields

Table I. Measured errors as function of grid size for several convection schemes

Scheme		20 × 20	40 × 40	80 × 80
UDS	$\phi_{\min}$	$9{\cdot}86 \times 10^{-7}$	$4{\cdot}62 \times 10^{-11}$	$6{\cdot}36 \times 10^{-19}$
	$\|1 - r_{\text{mass}}\|$	$3{\cdot}57 \times 10^{-1}$	$1{\cdot}80 \times 10^{-1}$	$7{\cdot}65 \times 10^{-2}$
	$\| \Delta\phi \|_\infty$	$8{\cdot}12 \times 10^{-1}$	$7{\cdot}73 \times 10^{-1}$	$6{\cdot}46 \times 10^{-1}$
	$\| \Delta\phi \|_2$	$6{\cdot}11 \times 10^{-3}$	$2{\cdot}59 \times 10^{-3}$	$1{\cdot}01 \times 10^{-3}$
QUICK	$\phi_{\min}$	$-5{\cdot}73 \times 10^{-2}$	$-1{\cdot}97 \times 10^{-2}$	$-2{\cdot}10 \times 10^{-4}$
	$\|1 - r_{\text{mass}}\|$	$2{\cdot}79 \times 10^{-2}$	$3{\cdot}21 \times 10^{-3}$	$3{\cdot}53 \times 10^{-4}$
	$\| \Delta\phi \|_\infty$	$3{\cdot}83 \times 10^{-1}$	$1{\cdot}54 \times 10^{-1}$	$4{\cdot}90 \times 10^{-2}$
	$\| \Delta\phi \|_2$	$2{\cdot}73 \times 10^{-3}$	$4{\cdot}96 \times 10^{-4}$	$7{\cdot}92 \times 10^{-5}$
Minmod	$\phi_{\min}$	$-3{\cdot}16 \times 10^{-5}$	$-5{\cdot}26 \times 10^{-8}$	$-2{\cdot}13 \times 10^{-19}$
	$\|1 - r_{\text{mass}}\|$	$4{\cdot}10 \times 10^{-2}$	$1{\cdot}21 \times 10^{-2}$	$3{\cdot}13 \times 10^{-3}$
	$\| \Delta\phi \|_\infty$	$6{\cdot}26 \times 10^{-1}$	$4{\cdot}48 \times 10^{-1}$	$2{\cdot}40 \times 10^{-1}$
	$\| \Delta\phi \|_2$	$4{\cdot}35 \times 10^{-3}$	$1{\cdot}20 \times 10^{-3}$	$2{\cdot}32 \times 10^{-4}$
ISNAS	$\phi_{\min}$	$-6{\cdot}46 \times 10^{-6}$	$-9{\cdot}33 \times 10^{-10}$	$-1{\cdot}16 \times 10^{-14}$
	$\|1 - r_{\text{mass}}\|$	$4{\cdot}44 \times 10^{-3}$	$1{\cdot}39 \times 10^{-3}$	$2{\cdot}24 \times 10^{-4}$
	$\| \Delta\phi \|_\infty$	$5{\cdot}25 \times 10^{-1}$	$3{\cdot}02 \times 10^{-1}$	$1{\cdot}36 \times 10^{-1}$
	$\| \Delta\phi \|_2$	$3{\cdot}50 \times 10^{-3}$	$7{\cdot}14 \times 10^{-4}$	$1{\cdot}18 \times 10^{-4}$
SMART	$\phi_{\min}$	$-1{\cdot}40 \times 10^{-8}$	$-1{\cdot}45 \times 10^{-10}$	$-1{\cdot}84 \times 10^{-12}$
	$\|1 - r_{\text{mass}}\|$	$2{\cdot}17 \times 10^{-2}$	$3{\cdot}13 \times 10^{-3}$	$3{\cdot}52 \times 10^{-4}$
	$\| \Delta\phi \|_\infty$	$4{\cdot}63 \times 10^{-1}$	$2{\cdot}41 \times 10^{-1}$	$9{\cdot}99 \times 10^{-2}$
	$\| \Delta\phi \|_2$	$3{\cdot}00 \times 10^{-3}$	$5{\cdot}47 \times 10^{-4}$	$8{\cdot}62 \times 10^{-5}$

the smallest errors on all three grids, both in L_2- and L_∞-norm, whereas QUICK has the best L_2- and L_∞-norms.

Concerning the mass errors, these are mainly caused by the fact that at the inflow boundaries the exact fluxes are imposed, whereas at the outflow boundaries—mathematically correct—the fluxes are computed from the interior numerical solution. As a consequence, owing to discretization errors, the total net flux is not zero. Hence schemes which are strictly conservative do not show strictly conservation behaviour for this test case unless—mathematically incorrect—the exact fluxes are also imposed at outflow. According to Vreugdenhil and Koren,[15] a scheme has good mass conservation properties if the corresponding mass error behaves like $\| \Delta\phi \|_2$. This is true for all schemes discussed and hence they are all sufficiently mass-conservative.

The positively error $\phi_{\min}$ indicates whether a given scheme guarantees positivity of the solution. UDS is truly positive, whereas QUICK is not. As a consequence, this scheme exhibits spurious oscillations. Owing to machine precision, the limiters do not completely avoid negative values, since limiters are not turned on exactly at the moment they should be. Even so, their convergence to machine precision is very fast, especially Minmod. Hence they are practically positive.

4.2. Advection of scalar step profile by rotational velocity field

The next linear test case is the advection of a step profile by a rotational velocity field, proposed by Smith and Hutton[16] and particularly designed for testing convection schemes. The problem is described by

$$u\frac{\partial\phi}{\partial x}+v\frac{\partial\phi}{\partial y}=\frac{1}{Pe}\left(\frac{\partial^2\phi}{\partial x^2}+\frac{\partial^2\phi}{\partial y^2}\right),\quad (x,y)\in[-1,1]\times[0,1], \tag{42}$$

where Pe is the Peclet number and the flow field is given by

$$u=2y(1-x^2),\qquad v=-2x(1-y^2). \tag{43}$$

The following boundary conditions are used:

$$\begin{aligned}
&\phi=1+\tanh[10(2x+1)], && y=0,\ -1\leqslant x\leqslant 0,\\
&\partial\phi/\partial y=0, && y=0,\ 0\leqslant x\leqslant 1,\\
&\phi=1-\tanh(10), && x=1,\ 0\leqslant y\leqslant 1,\\
&\phi=1-\tanh(10), && y=1,\ -1\leqslant x\leqslant 1,\\
&\phi=1-\tanh(10), && x=-1,\ 0\leqslant y\leqslant 1.
\end{aligned} \tag{44}$$

Computations are carried out on a uniform (x, y) grid of 40 × 20 with $Pe=10^6$ and the results are given in Figure 9. It can be seen that Minmod leads to somewhat more smeared contour lines than QUICK and other monotone schemes, whereas UDS produces too much numerical diffusion, leading to a highly smeared solution. The wiggles in Figure 9 are produced by the plotting software.

Figure 10 shows the performance of UDS, QUICK, Minmod, ISNAS and SMART by comparing the profiles at $x=0{\cdot}0$ obtained with these schemes. As expected, UDS is strongly affected by numerical diffusion and QUICK produces under- and overshoots, whereas other schemes are free from oscillations. Furthermore, ISNAS is less diffusive than Minmod but moderately more diffusive than SMART. Both ISNAS and SMART preserve the third-order accuracy of QUICK.

Concerning the computational costs required on an HP 9000/735 workstation, results are given in Table II. ISNAS requires about 20% more computation time than QUICK, whereas Minmod and SMART respectively consumed about 6% and 10% more time than ISNAS.

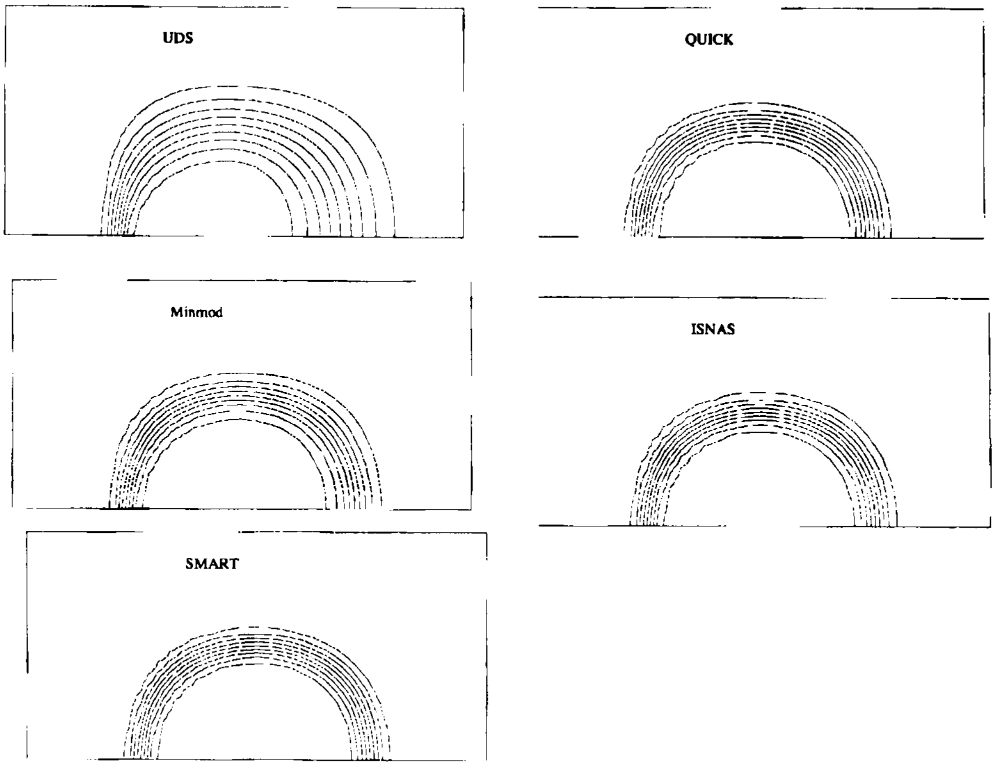

Figure 9. Contour plots of scalar property obtained with several convection schemes

4.3. Turbulent flow through a constricted tube

The main motivation for constructing and employing the ISNAS scheme is to approximate convective transport of turbulence quantities, particularly k and ε, very accurately while preserving positivity of k and ε. Numerical experiments have shown that non-monotone higher-order schemes are prone to generate negative values of turbulence quantities, particularly in regions where the gradients of those quantities are relatively high. Negative values of k and/or ε not only make the mathematical model physically meaningless but can also make the discretized equations highly unstable and hence prevent convergence to steady state.

In this subsection we examine the sensitivity with respect to the accuracy with which turbulence convection is approximated using the UDS and ISNAS schemes. The inertia terms in the momentum equations have been approximated with central differences. The numerical framework as described in Section 3 has been applied to the prediction of turbulent flow through a tube with a sinusoidal constriction, as shown in Figure 11. This flow has been studied experimentally by Deshpande and Giddens.[17]

The height of the duct is 50·8 mm and the Reynolds number based on that height and the average inlet velocity is 15,000. The height and base length of the constriction are $\frac{1}{2}R_0$ and $4R_0$ respectively, where R_0 is the half-height of the duct. Owing to symmetry, only the lower half of the domain needs to be considered (i.e. $y \in [-R_0, 0]$). The inlet profiles for the velocity and turbulence quantities were

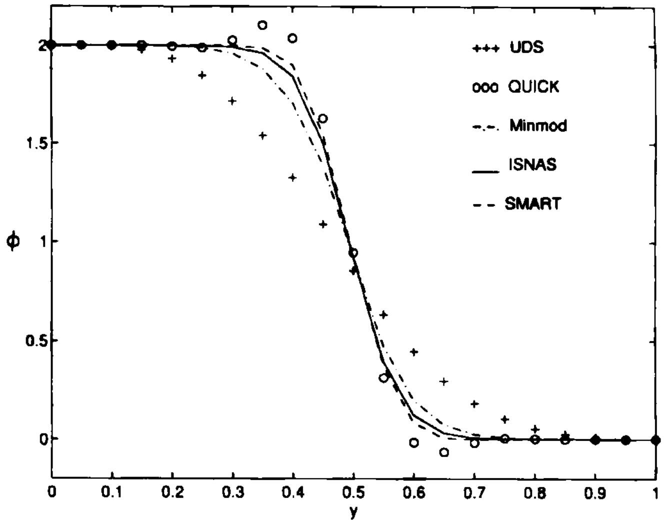

Figure 10. Comparison between various convection schemes—profiles at $x = 0$

specified at the plane $x = -4R_0$. Following Deshpande and Giddens,[17] at the inlet a fully developed power-law profile ($n \approx 6{\cdot}4$) is assumed for the streamwise velocity:

$$u_{\text{in}} = u_0\left(1 + \frac{y}{R_0}\right)^{1/6{\cdot}4}, \tag{45}$$

where u_0 is the centreline velocity. For the turbulence quantities k and ε the following inlet profiles are assumed:

$$k_{\text{in}} = 1{\cdot}5 I_{\text{T}}^2 u_{\text{in}}^2, \qquad \varepsilon_{\text{in}} = \frac{c_\mu^{3/4} k_{\text{in}}^{3/2}}{l}. \tag{46}$$

Here I_{T} is the turbulence intensity, taken to be 5%, and l is the mixing length given by

$$l = \min(\kappa(R_0 + y), 0{\cdot}1R_0). \tag{47}$$

In addition, symmetry and outflow conditions are imposed in the usual way.

Grid dependence tests have been performed with four grids consisting of 50 × 20, 75 × 30, 100 × 60 and 150 × 100 cells respectively. Figure 12 shows the 50 × 20 grid. The test focused primarily on the separation and reattachment lengths. The computed separation and reattachment lengths are presented

Table II. Measured computational costs for various convection schemes

Scheme	Iterations	CPU time (s)	CPU per iteration (s)	CPU ratio
UDS	7	1·53	0·22	1·00
QUICK	17	4·36	0·26	1·18
Minmod	10	3·28	0·33	1·50
ISNAS	14	4·35	0·31	1·41
SMART	23	7·80	0·34	1·55

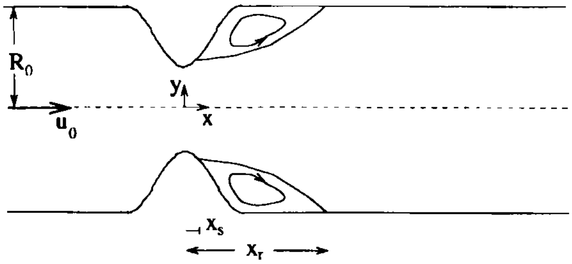

Figure 11. Geometry of solution domain for constricted tube flow

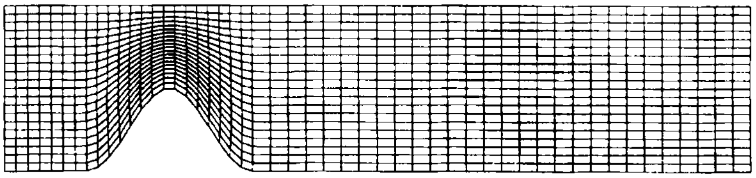

Figure 12. Typical grid for constricted tube flow (50 × 20 cells)

together with the measurements in Table III. The standard k–ε model gives an overpredicted separation length and underpredicted reattachment length. Furthermore, this table shows that no significant differences between the solutions obtained with UDS and ISNAS are found. The differences between the results obtained on the two finest grids are very small, suggesting that further mesh refinement is not necessary. Hence all subsequent computations were done with a 150 × 100 grid. With respect to the UDS and ISNAS schemes it appears that with $\Delta t = 0{\cdot}005$ s typically 445 and 435 time steps respectively were needed to obtain stationary solutions. The total CPU times were around 50 and 64 min respectively on the HP workstation. Hence with respect to UDS the CPU time per time step corresponding to ISNAS is about 30% higher.

In numerical experiments with this flow it was observed that the QUICK scheme gives rise to oscillations in sharp gradient regions, which lead to negative values of k and ε. Owing to non-linearities and coupling, these negative values tend to be enlarged, which eventually prevents convergence. Figure 13 illustrates this divergence and indicates that the computation suddenly stops after 60 time steps. Note that the L_2-norm on the change of the solution k between successive time steps is not the termination criterion used for obtaining stationary solutions but is only used to give a qualitative picture of the convergence behaviour of the calculation. The ISNAS scheme does not adversely affect the convergence behaviour.

Figures 14–17 show the streamwise velocity and turbulence intensity predictions at two stations. The calculation is seen to yield relatively good agreement with the measurements, except with respect to the turbulence intensity.* Here again, solutions (velocities as well as turbulence intensities) obtained with UDS and ISNAS were found to be virtually identical. Apparently, the solutions are insensitive to the accuracy of the approximation of the convective terms in the k–ε model, contrary to what is sometimes believed. A possible explanation is the fact that the convection mechanism is of minor importance to the balance of turbulent processes, in which production and dissipation rates are dominant. While this is true in most cases, there are circumstances in which convection of turbulent energy dominates, e.g. the turbulent confined co-flow jet in a duct, which will be discussed in the next subsection.

---

* Though the experimental data with respect to the velocity fluctuation v'_{rms} were not available, the turbulence intensity is estimated by assuming that $v'_{\mathrm{rms}} \approx w'_{\mathrm{rms}}$.

Table III. Variation in separation and reattachment lengths with different grids and convection schemes

Case	Scheme	Grid	Separation x_s/R_0	Reattachment x_r/R_0
Experiment	—	—	0·5	4·0
Standard k–ε	UDS	50×20	1·17	2·90
	UDS	75×30	0·85	3·18
	UDS	100×60	0·59	3·61
	UDS	150×100	0·57	3·61
Standard k–ε	ISNAS	50×20	1·19	2·52
	ISNAS	75×30	0·86	3·21
	ISNAS	100×60	0·59	3·61
	ISNAS	150×100	0·58	3·62

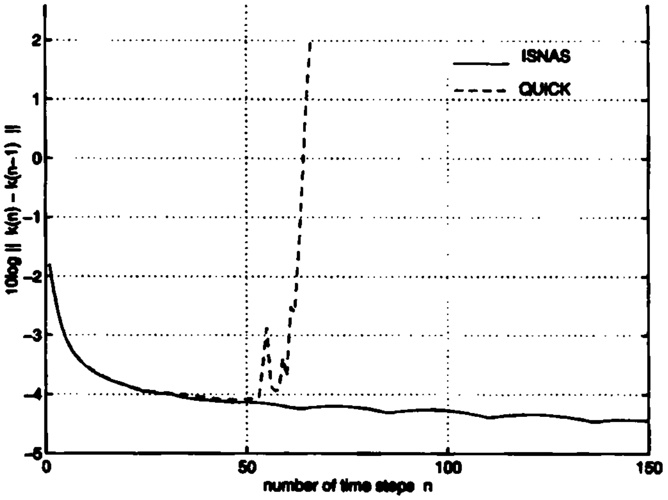

Figure 13. Convergence history of turbulent energy k of first 150 time steps

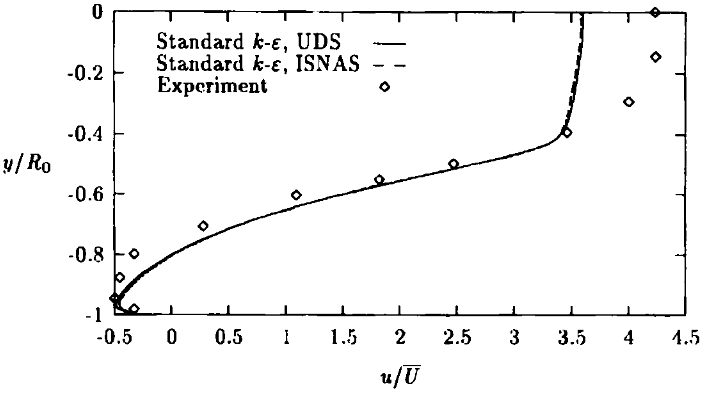

Figure 14. Streamwise velocity profile at $x/R_0=2{\cdot}0$

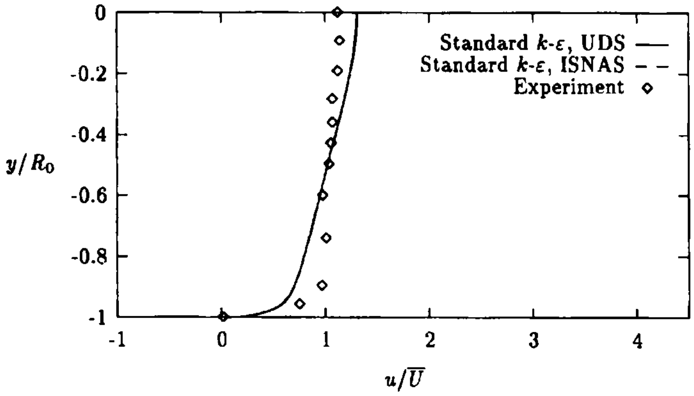

Figure 15. Streamwise velocity profile at $x/R_0 = 11{\cdot}0$

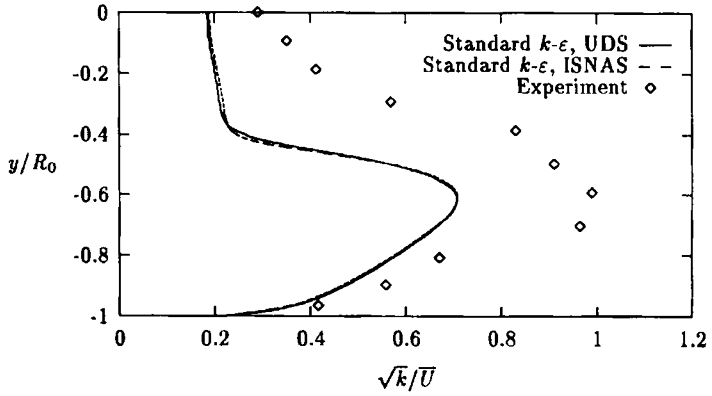

Figure 16. Turbulence intensity profile at $x/R_0 = 2{\cdot}0$

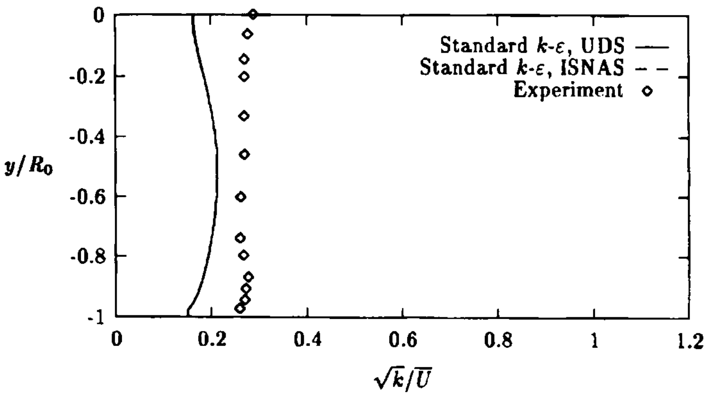

Figure 17. Turbulence intensity profile at $x/R_0 = 11{\cdot}0$

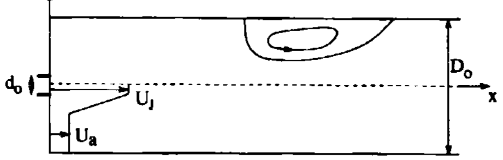

Figure 18. Flow configuration and definitions

4.4. Turbulent confined co-flow jet in a 2D planar duct

A typical flow in which convection of turbulence is relatively large is a turbulent co-flow jet or wake. Examples are plane and axisymmetric wakes of self-propelled bodies and confined co-flow jets in ducts or diffusers. There is experimental evidence that for this type of flow the turbulence convection prevails and is in balance with the dissipation rate, whereas the production rate is quite small (see e.g. Reference 18). This is also observed by Tennekes and Lumley,[19] for which they have examined the significance of several terms in the turbulent kinetic energy budget.

The test problem considered here is a turbulent co-flow jet in a planar duct. What the present computations are primarily intended to demonstrate is that the solutions, in particular the turbulence quantities, are quite sensitive to the accuracy of the approximation of the convection terms in the k–ε equations. A numerical study related to turbulent confined co-flow jets in a circular duct can be found in Reference 20, from which the specification and boundary conditions for this problem are taken and used in the present calculations. The geometry considered here is a symmetric planar duct with height D_0 and nozzle diameter d_0, as shown in Figure 18. In addition, U_J and U_a are the jet and ambient flow velocities respectively and $U_J/U_a = 31{\cdot}49$. Furthermore, $Re = U_J d_0/\nu = 1{\cdot}5 \times 10^5$. Computations were performed with the standard high-Re k–ε model in conjunction with wall functions on three different uniform grids, namely 50 × 40, 70 × 50 and 90 × 60 cells. Because of symmetry, computations are performed in half the domain only.

Figures 19 and 20 provide a comparison of turbulent viscosity profiles arising from the UDS and ISNAS schemes, both at location $x/D_0 = 1{\cdot}875$. These figures demonstrate that the turbulence quantities are rather sensitive to the convection schemes on turbulence equations adopted. Moreover, Figure 19 reveals a significant difference in the predicted profiles of μ_t corresponding to UDS. With the 70 × 50 mesh, grid-independent solutions for turbulent viscosity are achieved using ISNAS, whereas the

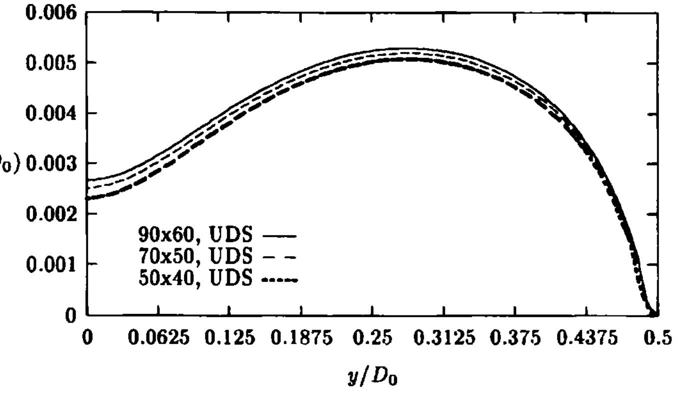

Figure 19. Effect of grid refinement on turbulent viscosity at $x/D_0 = 1{\cdot}875$

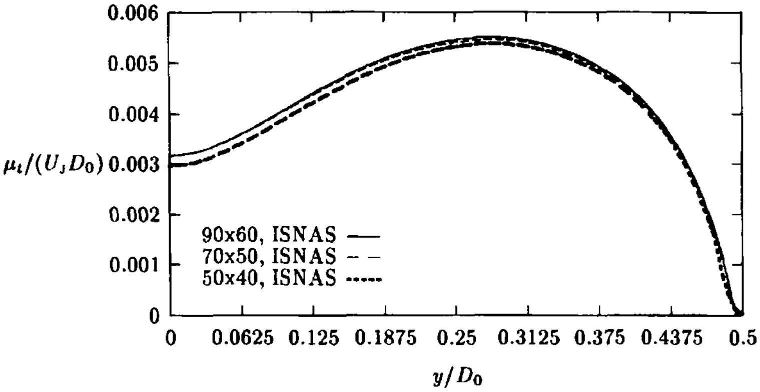

Figure 20. Effect of grid refinement on turbulent viscosity at $x/D_0 = 1{\cdot}875$

UDS solutions still had not reached the grid-independent stage. Thus ISNAS tends to minimize grid independence considerably. Moreover, like UDS, the ISNAS scheme does not exhibit unphysical oscillations. No negative turbulent energy or dissipation rate values are observed on all three grids.

In contrast with UDS, ISNAS does not result in severe numerical diffusion as seen in Figures 19 and 20, where the level of turbulent viscosity corresponding to UDS is lower than that of ISNAS. This can be explained as follows. In regions where shear stress is small, the production of turbulent energy and its dissipation rate are negligible. However, the dissipation terms in the transport equations of both k and ε remain non-zero. These terms must be in balance with the transport mechanism, in particular the convective transport. Hence it is important to approximate the convection of turbulence quantities accurately. When any numerical diffusion is introduced in the convection term (by UDS for example), this leads to a too high dissipation rate ε and, since ε is a sink term in the k-equation, to too low levels of turbulent energy. As a consequence, since μ_t is proportional to k^2/ε, this double-edged effect causes μ_t to become significantly too low.

The calculations with UDS and ISNAS schemes on the 70 × 50 grid both took 1500 time steps to converge and consumed respectively 102 and 135 CPU minutes. Hence the CPU time of the ISNAS scheme is about 30% higher than that of UDS.

5. CONCLUSIONS

A formally third order accurate flux-limited scheme for the approximation of convective transport in the finite volume context has been formulated using Leonard's NV concept. Since this formulation is simple and compact, it can be quite easily implemented in existing finite volume codes by employing the deferred correction procedure. It has been applied to a wide range of test cases, among them linear problems with discontinuous and smooth solutions and non-linear turbulent flow problems. The proposed scheme (ISNAS) appears to be satisfactory in the sense that

(i) it is oscillation free
(ii) it is practically second-order accurate (but third-order accurate on uniform grids)
(iii) it produces less numerical diffusion than Minmod but is a little more diffusive than SMART
(iv) it is generally applicable and robust
(v) the computational cost associated with the use of this scheme is modest: it requires about 30% more CPU time than the standard schemes (UDS and QUICK) but is cheaper than SMART.

The ISNAS scheme is suitable for approximation of advective transport in turbulence equations, e.g. the standard k–ε model, whose solutions must not, for reasons of stability, have non-physical negative values. However, in some situations this scheme leads to results which are no more accurate than those obtained with the first-order upwind scheme. A possible explanation is the fact that in such circumstances the balance of turbulent processes is dominated by the production and dissipation terms and hence the convective transport term is of minor importance. However, this need not always be the case, as shown in the previous section, and so one should always be aware of the inaccuracy of the first-order upwind scheme. Hence it is worthwhile to approximate convective turbulence transport with a higher-order monotone upwind scheme. In conclusion, when coarse grids are unavoidable, particularly in 3D situations, the use of a higher-order monotone upwind scheme becomes necessary if accuracy has to be improved.

ACKNOWLEDGEMENTS

This investigation was supported by the Netherlands Foundation for Mathematics SMC with financial aid from the Netherlands Organization for the Advancement of Scientific Research (NWO).

APPENDIX

Consider a limited upwind scheme (assuming that $u_1|_{(i+1/2,j)} > 0$; see Figure 1)

$$\phi_{(i+1/2,j)} = \phi_{(i,j)} + \tfrac{1}{2}\Psi(r)(\phi_{(i+1,j)} - \phi_{(i,j)}), \tag{48}$$

with

$$r = \frac{\phi_{(i,j)} - \phi_{(i-1,j)}}{\phi_{(i+1,j)} - \phi_{(i,j)}}. \tag{49}$$

We show that for any limiter Ψ which satisfies Sweby's monotonicity principle and makes (48) second-order accurate the following is true:

$$\left.\frac{\mathrm{d}\Psi}{\mathrm{d}r}\right|_{r=1} = \tfrac{1}{4} \iff \text{the scheme (48) is third-order accurate,} \tag{50}$$

assuming that the grid is uniform.

Suppose that the limited scheme (48) is third-order-accurate. We have

$$\Psi(r) \approx \Psi(1) + \Psi'(1)(r-1). \tag{51}$$

According to Sweby,[4] for any limiter Ψ which makes the scheme monotone and second-order accurate the following condition must hold:

$$\Psi(1) = 1. \tag{52}$$

Taylor expansion gives

$$\phi_{(i-1,j)} = \phi_{(i+1/2,j)} - \tfrac{3}{2}\Delta x_1\phi'_{(i+1/2,j)} + \tfrac{9}{8}\Delta x_1^2\phi''_{(i+1/2,j)} - \tfrac{27}{48}\Delta x_1^3\phi'''_{(i+1/2,j)} + \mathrm{HOT},$$

$$\phi_{(i,j)} = \phi_{(i+1/2,j)} - \tfrac{1}{2}\Delta x_1\phi'_{(i+1/2,j)} + \tfrac{1}{8}\Delta x_1^2\phi''_{(i+1/2,j)} - \tfrac{1}{48}\Delta x_1^3\phi'''_{(i+1/2,j)} + \mathrm{HOT},$$

$$\phi_{(i+1,j)} = \phi_{(i+1/2,j)} + \tfrac{1}{2}\Delta x_1\phi'_{(i+1/2,j)} + \tfrac{1}{8}\Delta x_1^2\phi''_{(i+1/2,j)} + \tfrac{1}{48}\Delta x_1^3\phi'''_{(i+1/2,j)} + \mathrm{HOT}.$$

Substituting the above expansions and equations (51) and (52) in scheme (48) and demanding that the scheme be third-order accurate, it is easily found that

$$\left.\frac{\mathrm{d}\Psi}{\mathrm{d}r}\right|_{r=1}=\tfrac{1}{4}. \tag{53}$$

Conversely, suppose the limiter Ψ makes the scheme (48) monotone and $\Psi'(1)=\frac{1}{4}$. We also have $\Psi(1)=1$. Using Leonard's normalized variable concept, it is possible to show that the scheme is third-order accurate. In terms of normalized variables, equation (48) becomes

$$\hat{\phi}_{(i+1/2,j)}=\hat{\phi}_{(i,j)}+\tfrac{1}{2}\Psi(r)(1-\hat{\phi}_{(i,j)}), \tag{54}$$

with

$$r=\frac{\hat{\phi}_{(i,j)}}{1-\hat{\phi}_{(i,j)}}. \tag{55}$$

This leads to

$$\frac{\mathrm{d}\hat{\phi}_{(i+1/2,j)}}{\mathrm{d}\hat{\phi}_{(i,j)}}=1-\tfrac{1}{2}\Psi(r)+\tfrac{1}{2}\frac{\mathrm{d}\Psi}{\mathrm{d}r}\frac{1}{1-\hat{\phi}_{(i,j)}}, \tag{56}$$

from which is easily found that

$$\frac{\mathrm{d}\hat{\phi}_{(i+1/2,j)}}{\mathrm{d}\hat{\phi}_{(i,j)}}=\tfrac{3}{4}\quad\text{at}\quad\hat{\phi}_{(i,j)}=\tfrac{1}{2}. \tag{57}$$

According to Leonard,[8] this is necessary and sufficient for third-order accuracy.

REFERENCES

1. B. P. Leonard, 'A stable and accurate convective modelling procedure based on quadratic upstream interpolation', *Comput. Methods Appl. Mech. Eng.*, **19**, 59–98 (1979).
2. G. D. Raithby, 'Skew upstream differencing schemes for problems involving fluid flow', *Comput. Methods Appl. Mech. Eng.*, **9**, 153–164 (1976).
3. A. Harten, 'High resolution schemes for hyperbolic conservation laws', *J. Comput. Phys.*, **49**, 357–393 (1984).
4. P. K. Sweby, 'High resolution schemes using flux limiters for hyperbolic conservation laws', *SIAM J. Numer. Anal.*, **21**, 995–1011 (1984).
5. C. Hirsch, *Numerical Computation of Internal and External Flows*, Vols 1 and 2, Wiley, Chichester, 1990.
6. P. Arminjon and A. Dervieux, 'Construction of TVD-like artificial viscosities on two-dimensional arbitrary FEM grids', *J. Comput. Phys.*, **106**, 176–198 (1993).
7. P. H. Gaskell and A. K. C. Lau, 'Curvature-compensated convective transport: SMART, a new boundedness-preserving transport algorithm', *Int. j. numer. methods fluids*, **8**, 617–641 (1988).
8. B. P. Leonard, 'Simple high-accuracy resolution program for convective modelling of discontinuities', *Int. j. numer. methods fluids*, **8**, 1291–1318 (1988).
9. P. Tamamidis and D. N. Assanis, 'Evaluation of various high-order-accuracy schemes with and without flux limiters', *Int. j. numer. methods fluids*, **16**, 931–948 (1993).
10. A. E. Mynett, P. Wesseling, A. Segal and C. G. M. Kassels, 'The ISNaS incompressible Navier–Stokes solver: invariant discretization', *Appl. Sci. Res.*, **48**, 175–191 (1991).
11. A. Segal, P. Wesseling, J. van Kan, C. W. Oosterlee and K. Kassels, 'Invariant discretization of the incompressible Navier–Stokes equations in boundary fitted co-ordinates', *Int. j. numer. methods fluids*, **15**, 411–426 (1992).
12. J. J. I. M. van Kan, 'A second-order accurate pressure correction method for viscous incompressible flow', *SIAM J. Sci. Stat. Comput.*, **7**, 870–891 (1986).

13. B. E. Launder and D. B. Spalding, 'The numerical computation of turbulent flows', *Comput. Methods Appl. Mech. Eng.*, **3**, 269–289 (1974).
14. M. Zijlema, A. Segal and P. Wesseling, 'Invariant discretization of the k–ε model in general co-ordinates for prediction of turbulent flow in complicated geometries', *Comput. Fluids*, **24**, 209–225 (1995).
15. C. B. Vreugdenhil and B. Koren (eds), *Numerical Methods for Advection–Diffusion Problems*, NNFM Vol. 45, Vieweg, Braunschweig, 1993.
16. R. M. Smith and A. G. Hutton, 'The numerical treatment of advection: a performance comparison of current methods', *Numer. Heat Transfer*, **5**, 439–631 (1982).
17. M. D. Deshpande and D. P. Giddens, 'Turbulence measurements in a constricted tube', *J. Fluid Mech.*, **97**, 65–89 (1980).
18. M. S. Uberoi and P. Freymuth, 'Turbulent energy balance and spectra of the axisymmetric wake', *Phys. Fluids*, **13**, 2205–2210 (1970).
19. H. Tennekes and J. L. Lumley, *A First Course in Turbulence*, MIT Press, Cambridge, MA, 1983.
20. J. Zhu and T.-H. Shih, 'Computation of confined coflow jets with three turbulence models', *Int. j. numer. methods fluids*, **19**, 939–956 (1994).